Ionics (2020) 26:33–42
https://doi.org/10.1007/s11581-019-03181-4

ORIGINAL PAPER

Microwave-assisted synthesis of $CuC_2O_4 \cdot xH_2O$ for anode materials in lithium-ion batteries with a high capacity

Zhiqiang Qi[1] · **Yuandong Wu**[1] · **Xiaofang Li**[1] · **Yi Qu**[1] · **Yongying Yang**[1] · **Dajiang Mei**[1]

Received: 28 March 2019 / Revised: 27 June 2019 / Accepted: 22 July 2019 / Published online: 3 August 2019

Abstract

Two $CuC_2O_4 \cdot xH_2O$-based anode materials with nanoscale microtopography were synthesized by microwave-assisted hydrothermal and solvothermal methods at 120 °C. These two compounds exhibit the higher electrochemical performance compared with other transition metal oxalate-based materials in lithium-ion batteries. The charge-discharge test results reveal that the electrochemical properties of copper oxalate hydrate are significantly better than those of the previous works without assistance of microwave. The quasi-spherical aggregates of $CuC_2O_4 \cdot xH_2O$ (x~0.14) possess the initial discharge capacity at 1436 mAh g^{-1} and the residual capacity at 1260.4 mAh g^{-1} after 100 cycles at 200 mA g^{-1}. On the other hand, the quasi-cotton aggregates of $CuC_2O_4 \cdot xH_2O$ (x~0.49) possess the initial discharge capacity at 1689 mAh g^{-1} and the residual capacity at 1181.1 mAh g^{-1} under the same conditions.

Keywords Microwave · Copper(II) oxalate · Anode material

Introduction

The reusable lithium-ion batteries (LIBs), as a significant electrochemical energy storage devices, have aroused worldwide concern for their varied applications such as mobile phone, notebook computer, new energy vehicle, and so on [1–3]. For the past decade, people have paid a high attention to improve the performance of LIBs [4–6]. As we know, graphite anode materials are used in most commercial LIBs. The graphite does not meet the requirements of future high-performance LIBs because its theoretical specific capacity is only 372 mAh g^{-1}. Hence, there is strong demand for developing new anode materials of LIBs with high reversible capacity, stable cycling life. Recently, silicon-titanium nanocomposites can also be obtained by molten salt electrolysis as anodes for LIBs, which have good electrochemical properties [7]. Nowadays, scientists have discovered several kinds of new anode materials to replace graphite, such as Si [8], Ge [9], $Li_4Ti_5O_{12}$ [10], SnO_2 [11], CuO [12], and transition metal oxalates (TMOxs) [13].

Recently, great progress has been made in the research of electrochemical properties of TMOxs [13, 14], such as MnC_2O_4 [15, 16], FeC_2O_4 [17, 18], CoC_2O_4 [19–23], NiC_2O_4 [17, 23], and ZnC_2O_4 [24]. The large volume change of the active material is a major factor leading to poor cycle performance during charging/discharging. In this aspect, the morphology, structure, or particle size has been deemed to a crucial factor to surmount the disadvantage of LIB anode material [25]. The ribbon-like nanosized FeC_2O_4 and CoC_2O_4 as LIB anode materials can give capacities of 700 mAh g^{-1} and 900 mAh g^{-1} at 2000 mA g^{-1}, respectively, after 40 cycles [26, 27]. The mesoporous FeC_2O_4 and CoC_2O_4 nanostructures prepared by chimie douce precipitation method exhibited smaller size. These results shown higher reversible capacity, more stable cycling, and better rate capabilities compared to those reported previously [18, 28]. Reasonable synthesis methods could be effective means to elevate their electrochemical performances. The SnC_2O_4/graphene composite was synthesized as the anode material of LIB by microwave-assisted method. The reversible discharge capacity was 657 mAh g^{-1} after 100 cycles at 200 mA g^{-1} [29]. Microwave-assisted methods significantly reduce particle size

---

Electronic supplementary material The online version of this article (https://doi.org/10.1007/s11581-019-03181-4) contains supplementary material, which is available to authorized users.

✉ Yuandong Wu
wuyuandong@sues.edu.cn

[1] College of Chemistry and Chemical Engineering, Shanghai University of Engineering Science, Longteng Road 333, Shanghai 201620, People's Republic of China

and reaction time, indicating potential application in actual production.

Herein, we report the microwave-assisted methods for the controlled synthesis of $CuC_2O_4{\cdot}xH_2O$-based anode materials by choosing suitable synthetic mediums (water and ethyl glycol). The quasi-spherical hydro-$CuC_2O_4{\cdot}xH_2O$ (*hCuOx*) and quasi-cotton solvo-$CuC_2O_4{\cdot}xH_2O$ (*sCuOx*) were obtained and the as-prepared $CuC_2O_4{\cdot}xH_2O$ nanostructures exhibited superior reversible specific capacity and cycling stability as the anode materials for LIBs. Their reversible specific capacity of *hCuOx* and *sCuOx* can be maintained as high as 1201 and 1008 mAh g^{-1} at the current density of 200 mA g^{-1} after 50 cycles, respectively.

Experimental

Materials

All chemicals were analytical grade and without further purification: EG (AR, Aladdin Industrial Corporation, 99%), $H_2C_2O_4{\cdot}2H_2O$ (GR, Aladdin Industrial Corporation, 99.8%), $CuCl_2{\cdot}2H_2O$ (AR, Aladdin Industrial Corporation), separator (Celgard 2400), electrolyte (EC:DMC:EMC=1:1:1+1%VC, Nanjing Mojiesi).

Synthesis of $CuC_2O_4{\cdot}xH_2O$ materials

The microwave reaction is carried out in the EXCEL full-function microwave chemistry working platform (PreeKem Shanghai). $CuCl_2{\cdot}2H_2O$ (s, 1.194 g, 7 mmol) was dissolved into 35 mL DI (or 35 mL EG). $H_2C_2O_4{\cdot}2H_2O$ (s, 0.883 g, 7 mmol) was added into the solution. After stirring for 1 h, the suspension was transferred into a 100-mL Teflon liner and heated at 120 °C for 20 min in a microwave system of EXCEL. The products *hCuOx* and *sCuOx* were collected by centrifugation. The precipitates were washed with DI and then ethanol (ET) three times and dried at 120 °C under vacuum for 12 h. The schematic diagram for the formation of *hCuOx* and *sCuOx* is shown in Scheme 1.

Characterization

The powder X-ray diffraction (XRD) data of both *hCuOx* and *sCuOx* were collected at room temperature on a Bruker D8 powder X-ray diffractometer equipped with Cu Kα radiation ($\lambda = 1.5418$ Å) in the 2θ range 5°–80°. Thermogravimetric (TG) analysis was performed on a SDTQ600 TG–DSC (TA Instruments) with a continuous 10 °C min^{-1} ramped from room temperature to 800 °C. The morphology of both samples were observed on a scanning electron microscope (SEM, Hitachi S-3400), transmission electron microscopy (TEM, JEM 2100), and high-resolution transmission electron microscopy (HRTEM, H-800). The dynamic light scattering (DLS) measurements were performed in MilliQ water using a Nano-s90 (Malvern Instruments, Worcestershire, UK).

Electrochemical experiments

The working electrodes were prepared with active materials, acetylene black and polyvinylidene fluoride (PVDF) by the proportion of 7:2:1, and the solvent was 1-methyl-2-pyrrolidone. The slurry was smeared on a copper foil (wetting thickness: 150 μm, 1 mg) and dried in a vacuum oven at 80 °C for 12 h. Lithium metal was used as a counter electrode, and a carbon copper foil was coated as a counter current collector, and glass fibers were used as a separator and an electrolyte. The cells' charge/discharge tests on XINWEI CT-4008 system (Shenzhen Neware Battery, China) with range of 0.01–3.0 V. Cyclic voltammograms (CVs) were measured on electrochemical workstation (CHI-660e, Huachen, Shanghai) with range 0.01–3.0 V at a scan rate of 0.1 mV s^{-1}.

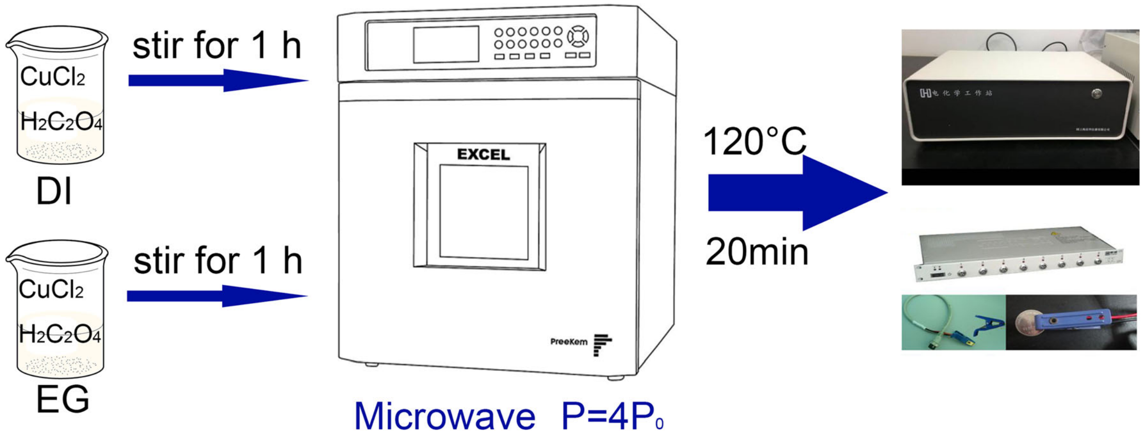

Scheme 1 The synthesis illustration of $CuC_2O_4{\cdot}xH_2O$ obtained by facile microwave solvothermal reactions and electrochemical performance test

Results and discussion

Characterization of $CuC_2O_4{\cdot}xH_2O$

Figure 1a shows XRD patterns of orthorhombic $CuC_2O_4{\cdot}xH_2O$ ($0 < x < 1$) (JCPDS 21-07). The widths of all diffraction peaks are quite broad demonstrating. According to the Debye-Scherrer equation [30], the calculated interplanar spacing of (110) faces can be treated as an equivalent for the average size of primary nanocrystals, giving a value of 8.9 and 14.1 nm for *hCuOx* and *sCuOx*, respectively. As shown in Fig. 1b, the peaks below 1000 cm^{-1} correspond to typical Cu–O vibrations, and the bands at 1322–1600 cm^{-1} are attributed to the C=C vibrations [31]. From the results about Raman spectra (Fig. S1), it can be found that the characteristic main peaks of these two materials are almost identical [32].

TGA/DSC measurements were performed to estimate the weight of crystallized water and the structural stability of $CuC_2O_4{\cdot}xH_2O$ (Fig. 1c, d). Although it is hard to clearly distinguish thermal and oxygen decomposition at a heating step of 10 °C/min^{-1} , the decomposition of *hCuOx* and *sCuOx* were carried out in two steps. The release of crystallized water molecules and decomposition of anhydrous copper oxalate can be described by Eqs. (1) and (2) [20, 33]. From Fig. 1d, the thermal dehydration and oxalate decomposition processes occurred at ca. 260 °C and 320 °C, respectively.

$$CuC_2O_4 \cdot xH_2O \rightarrow CuC_2O_4 + xH_2O \qquad (1)$$

$$CuC_2O_4 \rightarrow Cu + 2CO_2 \qquad (2)$$

The TGA/DSC result suggests that the total weight loss of *hCuOx* and *sCuOx* were 58.7% and 60.4%, and the corresponding x values were 0.14 and 0.49, respectively [34].

The surface properties and porosity of the *hCuOx* and *sCuOx* were further investigated by N_2 adsorption measurements. The Brunauer, Emmett, and Teller (BET) tests were also performed to analyze the pore size distribution. The Barrett, Joyner, and Halenda (BJH) pore size distribution and the type IV N_2 adsorption/desorption isotherm curves of *hCuOx* and *sCuOx* are exhibited in Fig. 2a, b, respectively. N_2 adsorption/desorption isotherms have weak hysteresis loop at the relative pressure of 0.7–1.0 P/Po. As Fig. 3a shows, these average pore diameters for *hCuOx* and *sCuOx* are determined at 10.4 nm and 15.4 nm, which indicated mainly mesopores. The BET surface area of *sCuOx* (50.5 $m^2\ g^{-1}$) is larger than that of *hCuOx* (15.4 $m^2\ g^{-1}$). The *hCuOx* and *sCuOx* show larger pore sizes compared to the results of other copper compounds and other oxalates listed in Table 1. Furthermore, the large porous is of beneficial help for providing more active sites for quick electron transfer at the electrolyte/electrode interface, which results in huge improvement of electrochemical performance [37].

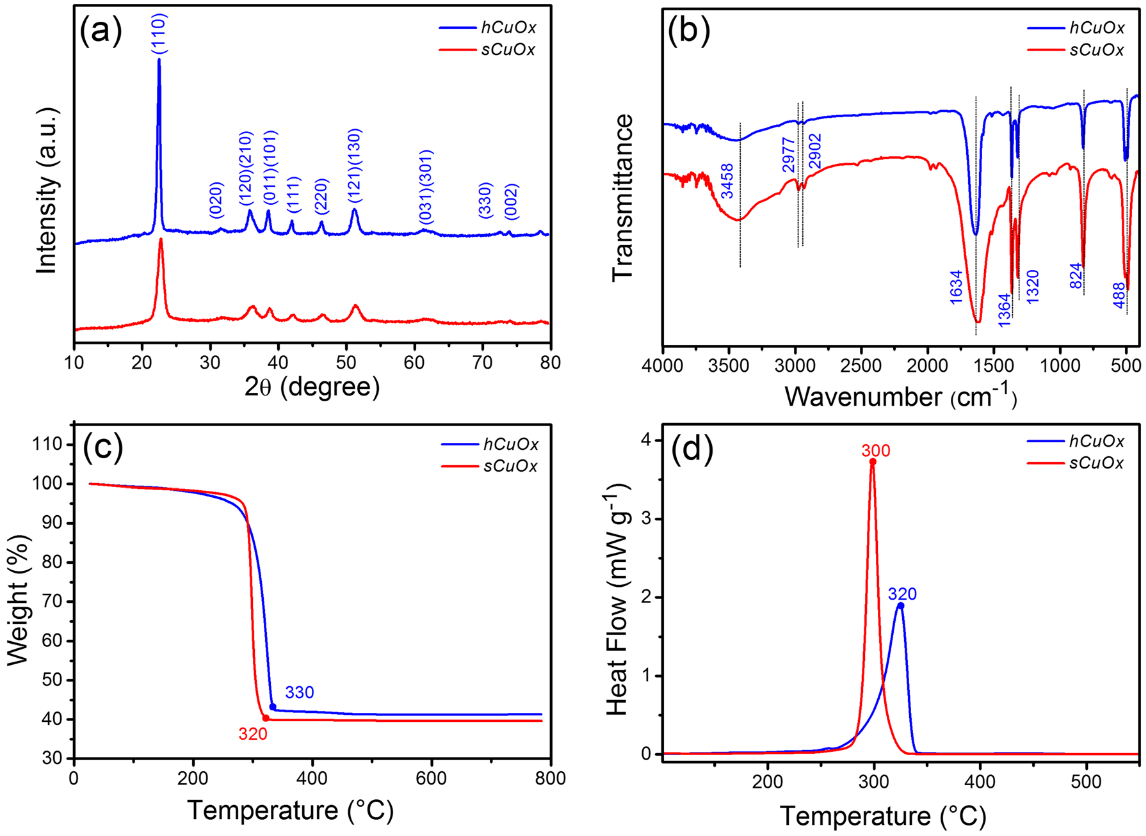

Fig. 1 **a** XRD patterns, **b** FT-IR spectra, **c** TGA and **d** DSC of *hCuOx* and *sCuOx*

Fig. 2 **a** BJH pore size distribution and **b** N_2 adsorption-desorption isotherms curves of *hCuOx* (up) and *sCuOx* (below)

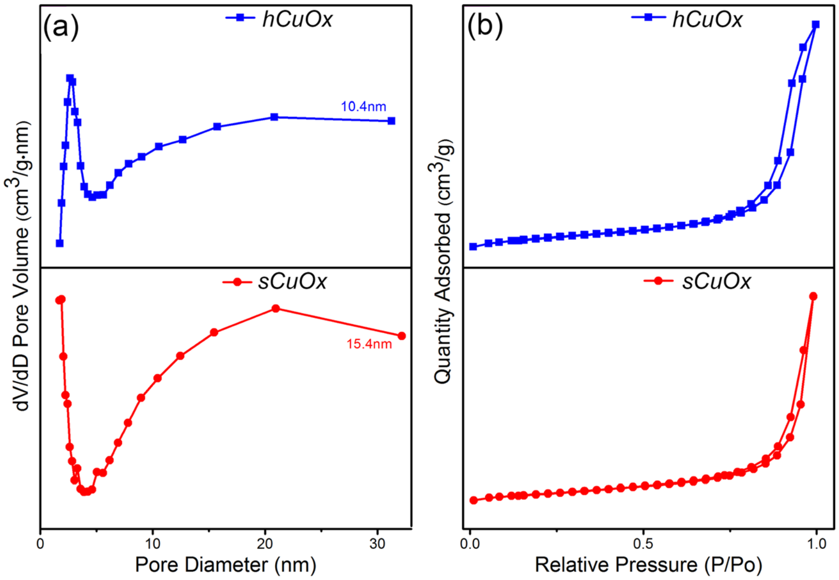

As shown in Fig. 3, the SEM images clearly present the considerable difference in the morphology between the *hCuOx* and *sCuOx*. The *hCuOx* has a quasi-spherical morphology with diameter of ca. 200–600 nm. The *sCuOx* has quasi-cotton morphology (Fig. 3c, d) with an average size of ca. 50 nm. The results demonstrate that the reaction mediums can control growth of these materials with different shapes. Compared to the resistance heating method, microwave-assisted heating method has several advantages: (i) uniform particle size; (ii) the particle size of hydrated copper oxalate decreased obviously; (iii) the morphology has changed dramatically [38, 39].

Further investigation of both $CuC_2O_4·xH_2O$ morphologies were performed by TEM experiments. The *hCuOx* and *sCuOx* revealed the quasi-spherical shape (Fig. 4a, b) and the quasi-cotton morphology (Fig. 4d, e), respectively. The electron beam was focused on the $CuC_2O_4·xH_2O$ nanoparticles, and TEM observations present the ambiguous lattice fringes that are amplified and shown as inset in Fig. 4b, e. The HRTEM images of *hCuOx* exhibited in Fig. 4c reveal a distinct set of visible lattice fringes with interplanar spacing of 0.17 nm and 0.23 nm, corresponding to the (020) and (111) planes of orthorhombic $CuC_2O_4·xH_2O$, respectively. Similarly, the HRTEM image of *sCuOx* is displayed in Fig. 4f with the

Fig. 3 **a**, **b** SEM images of *hCuOx* at different magnifications and **c**, **d** SEM images of *sCuOx* under the same condition

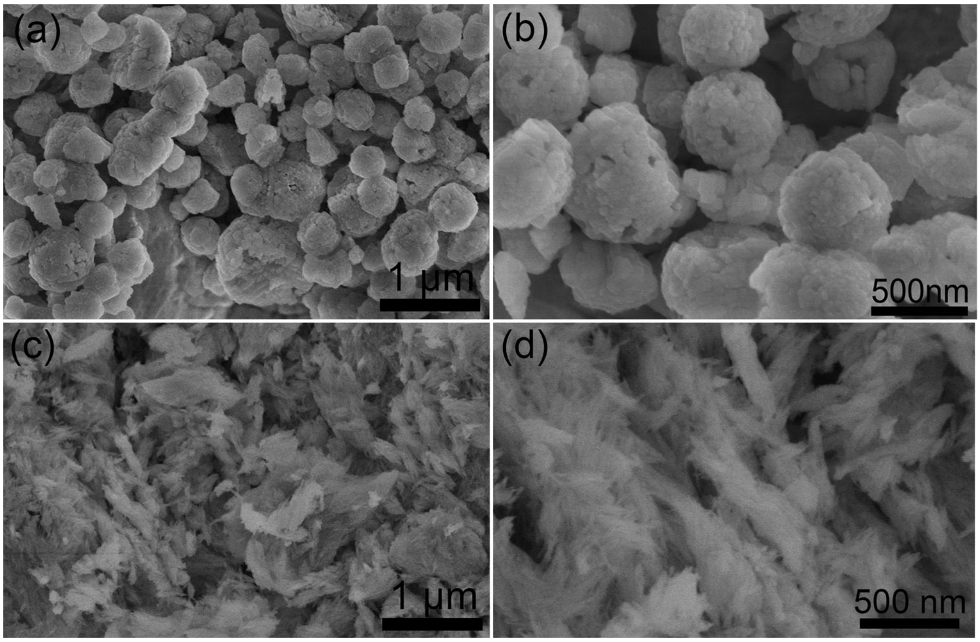

Table 1 Comparison of the surface and textural properties of $CuC_2O_4 \cdot xH_2O$ materials between this work and the previous reports

No.	Material	Morphology	Specific surface area ($m^2\ g^{-1}$)	Average pore diameter (nm)	Ref.
1	*hCuOx* (*x*-0.14)	Nanospheres	15.4	10.4	This work
2	*sCuOx* (*x*-0.49)	Nanorods	50.5	15.4	This work
3	$CuC_2O_4 \cdot 0.5H_2O$	Nanoribbons	30	–	[17]
4	CoC_2O_4	Nanobundles	33.1	3.6	[22]
5	SnC_2O_4/rGO	Nanocomposites	19.6	2	[29]
6	CuO/rGO	Nanocomposites	23.6	3.3	[35]
7	$CuCo_2S_4$/rGO	Nanocomposites	32.28	–	[36]

(020) and (120) planes corresponding to interplanar spacing of 0.17 and 0.20 nm.

As shown in Fig. S2, the dynamic light scattering (DLS) results reveal that the average hydrodynamic sizes of *hCuOx* and *sCuOx* are about 712 and 255 nm, respectively. The results are larger than the data (400 and 50 nm) observed in TEM and SEM analyses (Figs. 3 and 4). This is mainly due to the fact that the TEM and SEM images exhibited the actual size, whereas the size measured by the DLS method is the hydrodynamic diameter in the hydrated state [40].

Electrochemical characterization

Cyclic voltammetry (CV) curves are shown in Fig. 5. The $CuC_2O_4 \cdot xH_2O$ first degrade to Cu and Cu_2O, which are subsequently involved in conversion reactions. The reaction mechanism of TMOxs (such as iron [18], cobalt, and nickel oxalates [23]) can be described via Eq. (3). The incipient reaction of $CuC_2O_4 \cdot xH_2O$ with lithium can be roughly described as Eq. (4).

$$MC_2O_4 + 2Li^+ + 2e^- \rightarrow Li_2C_2O_4 + M \tag{3}$$

$$CuC_2O_4 \cdot xH_2O + Li^+ + e^- \rightarrow Cu_2O + Cu + Li_2CO_3 + Li_2O + LiOH \tag{4}$$

As shown in Fig. 5a, two cathodic current peaks at 1.42 and 0.86 V in the first cycle are observed. The high peak located at 0.86 V in the first cycle transferred to 1.05 V during the second cycle. Figure 5b presents CV behaviors of *sCuOx* electrode, which indicates two cathodic current peaks at 1.21 and 0.89 V, then the peak located at 0.89 V in the first cycle shifted to 1.03 V, finally, deracinated in the following cycle. This boils down to the following reasons: (i) the decomposition

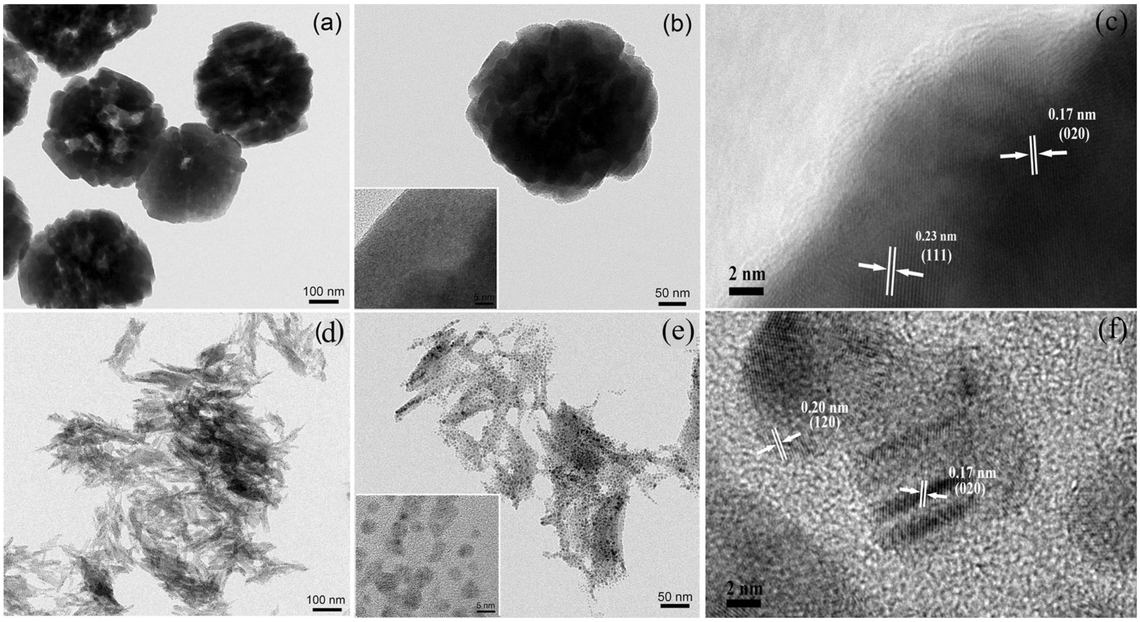

Fig. 4 TEM images (**a**, **b**) of *hCuOx* and TEM images (**d**, **e**) of *sCuOx*. Inset is the corresponding lattice fringes of a representative nanoparticle and HRTEM image (**c**) of *hCuOx* and HRTEM image (**f**) of *sCuOx*

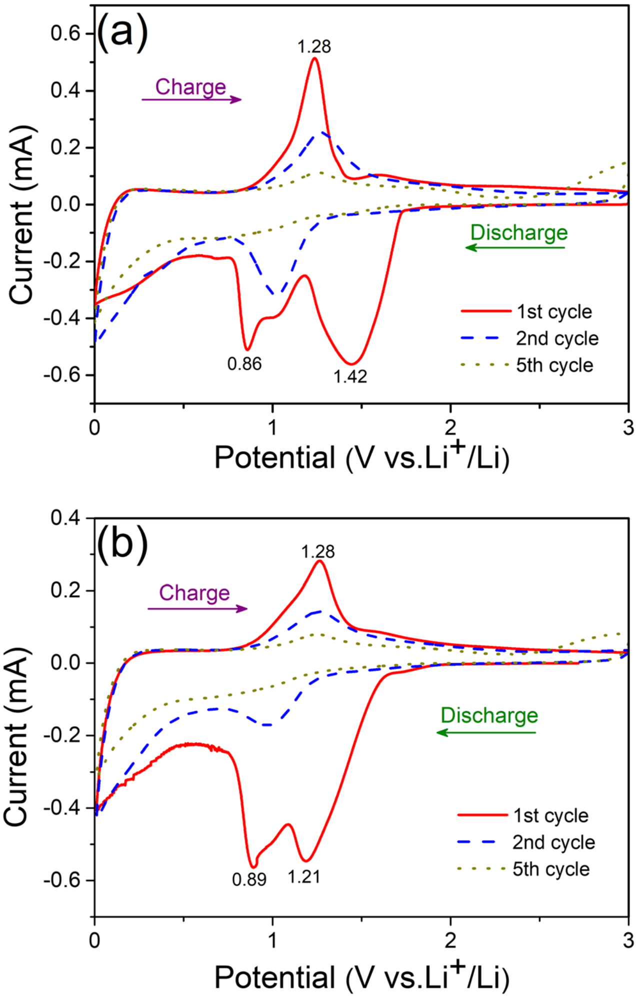

Fig. 5 CV profile at 0–3 V at a scan rate of 0.1 mV s^{-1}: **a** *hCuOx* and **b** *sCuOx*

of electrolyte leads to the formation of an organic layer deposited on the surface of the particles; (ii) lithium-ion intercalation conversion reaction from Li_2CO_3, Li_2O, LiOH, Cu_2O, and metallic copper (Cu^0) particles as shown in Eq. (4). Meanwhile, an oxidation peak in 1.28 V was noted during the anodic process, same as the reversible oxidation step of Cu^0, Cu^+ to Cu^{2+}. Figure 5b displays CV behaviors of *sCuOx* electrode, which manifests the same lithium storage mechanism as that of *hCuOx* [24, 33].

Figure 6 presents the voltage profile and the cycling behavior of the samples at 200 mA g^{-1}. The *hCuOx* electrode materials manifested the incipient discharge potential plateau at ~ 1.5 V, then thin slope corresponding to the electrochemical reaction of $CuC_2O_4{\cdot}xH_2O$ with lithium. From Fig. 6a, initial discharge capacity of *hCuOx* electrode is 1436.2 mAh g^{-1} and charge capacity is 819.1 mAh g^{-1} with a coulombic efficiency of 57% (Fig. 6a). A significant irreversible capacity loss in the first cycle is due to secondary reactions, such as the electrochemical removal process of crystallized water and the decomposition of electrolyte to form solid electrolyte interphase (SEI) layers on the surface of electrode. The prominently decay of capacity to the four full cycles due to electrochemical properties of $CuC_2O_4{\cdot}xH_2O$ $(0 < x < 1)$. Subsequently, the *hCuOx* gives discharge capacities of 495.7, 809.6, 1040.8, and 1192.3 mAh g^{-1} for the 4th, 10th, 20th, and 50th cycles, respectively. Every reversible cycle reveals high Coulomb efficiency about 97.6% (Fig. 6b). In order to explore the effect of charge and discharge on morphology, we monitored the changes in morphology of the two $CuC_2O_4{\cdot}xH_2O$ materials before cycling test. Fig. S3 gives the SEM images of fresh electrode and the electrode after 50 charge/discharge cycles at the current density of 200 mA g^{-1}. Comparing with the fresh electrode, the electrode after 50 charge-discharge cycles shows some microstructure changes. This indicates that the two electrode materials are relatively stable.

Compared with the electrochemical data displayed in Fig. 6a, b, *sCuOx* electrode indicates higher initial discharge capacity of 1688.1 mAh g^{-1} and slightly lower charge capacity of 634.3 mAh g^{-1}, with a lower initial Coulomb efficiency of 37.6% (Fig. 6c). At the same time, a recovery for the lithium storage capability of *sCuOx* is relatively low after the first 4 cycles and displays the 4th, 10th, 20th, and 50th cycle discharge capacity of 521.1, 780.7, 992.5, and 1024.1 mAh g^{-1}, respectively (Fig. 6b). Both the initial and 50th discharge capacities of *hCuOx*/*sCuOx* electrodes are outclass commercial graphite (372 mAh g^{-1}).

To further explore the cycling stability and rate cycling performances of *hCuOx* and *sCuOx*, the discharge capacities at 200 or 500 mA g^{-1} are shown in Fig. 7a. The discharge-charge curves of *hCuOx* and *sCuOx* at 1000 mA g^{-1} are given in Fig. S4. In the case of *hCuOx*, it is observed that the capacity fades up to four cycles and starts to increase thereafter. A maximum discharge capacity of 1263.2 mAh g^{-1} is observed at the 30th cycle and 200 mA g^{-1} rate, and the capacity gradually decreases with prolonging time. With the increase of current density, the charge/discharge capacity of *hCuOx* decreased obviously. At a rate of 500 mA g^{-1}, the maximum discharge capacity was 1209.1 mAh g^{-1} at the 38th cycle, and then the capacity was gradually decayed. After 100 cycles, the cells deliver stable reversible capacity of 1260.4 and 1064.3 mAh g^{-1} at 200 and 500 mA g^{-1} rate, respectively. At a current density of 1000 mA g^{-1} (Fig. S5), the 100th discharge capacities for *hCuOx* and *sCuOx* are 780.2 and 624.6 mAh g^{-1}, respectively.

In Fig. 7a, at each current density, the higher initial discharge capacity and lower capacity retention of *sCuOx* are shown. The discharge capacity decreases in the first four cycles and then increases continuously, the same as those of the *hCuOx*. If the current density is 500 mA g^{-1}, the 100th discharge capacities are 1064.3 mAh g^{-1} (*hCuOx*) and 939.3 mA h g^{-1} (*sCuOx*). Compared to the previously reported results of CuO-based anode materials and other dehydrated

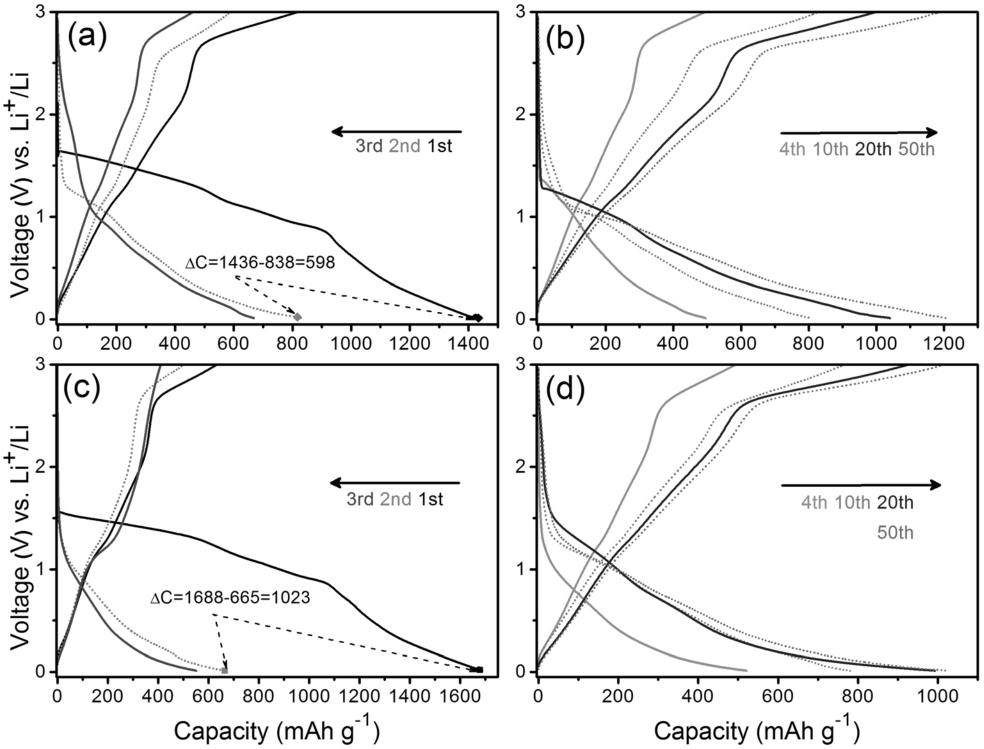

Fig. 6 Discharge-charge profiles of **a**, **b** *hCuOx* and **c**, **d** *sCuOx* electrodes operated at 200 mA g^{-1}

oxides listed in Table 2, the charge/discharge capacities of $CuC_2O_4{\cdot}xH_2O$ materials are also very excellent.

To check the rate capability, the *hCuOx* and *sCuOx* electrodes were cycled 10 times from 100 to 2000 mA g^{-1} (Fig. 7b). The cells were charged and discharged at different current densities of 100, 200, 500, 1000, and 2000 mA g^{-1} within a voltage range of 0.01–3.0 V. Both *hCuOx* and *sCuOx* electrodes undergo an initial reduction followed by a continuous increase in discharge capacity. A comparison of *hCuOx* (x~0.14) with *sCuOx* (x~0.49) at different current densities shows that the *hCuOx* nanostructures have lower initial discharge capacity and larger capacity decay at current densities

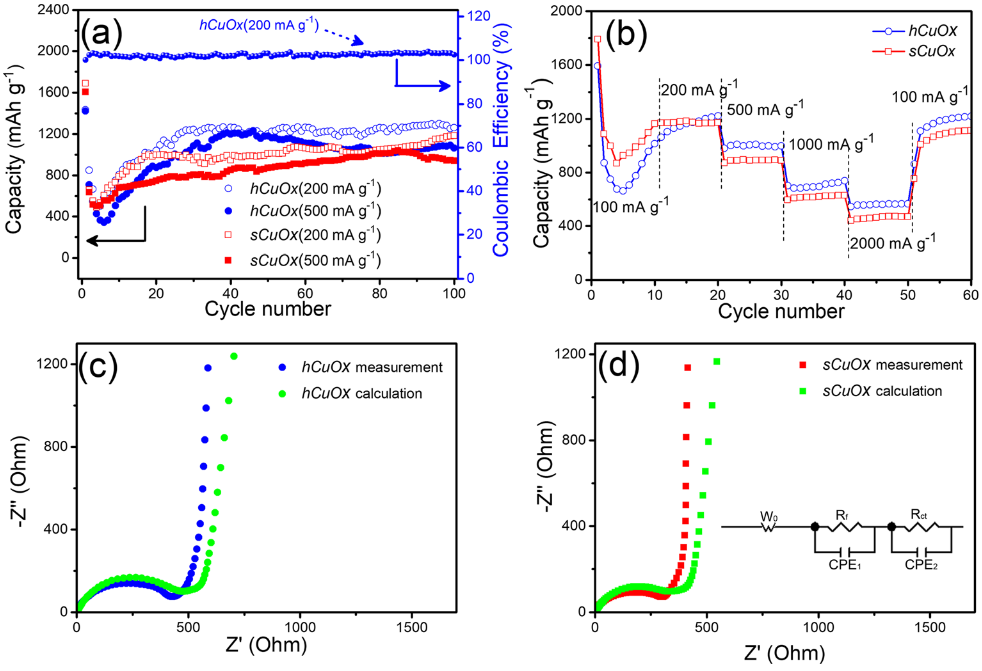

Fig. 7 **a** Cycling performance measured at 200 mA g^{-1} and 500 mA g^{-1}. **b** Rate capability at various current densities. **c**, **d** EIS of *hCuOx* and *sCuOx*

Table 2 A summary for the lithium storage capability of as-prepared $CuC_2O_4{\cdot}xH_2O$ nanostructures, dehydrated oxysalts, and CuO-based anode materials reported previously

Material	Morphology/size	Current	Residual capacity (mAh g^{-1})	Ref.
hCuOx (x~0.14)	Quasi-spherical/~ 200 nm	200 mA g^{-1} 500 mA g^{-1}	1260.4/100th cycle 1064.3/100th cycle	This work
sCuOx (x~0.49)	Quasi-rod/~ 50 nm	200 mA g^{-1} 500 mA g^{-1}	1181.1/100th cycle 939.3/100th cycle	This work
$CuC_2O_4{\cdot}0.5H_2O$	Nanorod/~ 20 nm	1C 2C 5C	200/70th cycle 200/70th cycle 200/70th cycle	[17]
MnC_2O_4	Nanoribbon/~ 200 nm	2C	250/70th cycle	[15]
FeC_2O_4	Nanoribbon/unknown	2C	480/70th cycle	[18]
CoC_2O_4	Nanoribbon/~ 30 nm	2C	700/70th cycle	[20]
CuO	Nanoparticle/~ 30 nm	1348 mA g^{-1}	665.8/70th cycle	[31]
CuO/graphene	Granule/~ 30 nm	67 mA g^{-1}	583.5/70th cycle	[35]

C = 1 Li h^{-1} mol^{-1}

of 100 and 200 mA g^{-1}. Thus, higher capacity increase ensues, thereafter, higher capacity maintainability at current densities of 500, 1000, and 2000 mA g^{-1}. Finally, the current density is set back to 100 mA g^{-1} and *hCuOx* and *sCuOx* are still found to deliver high discharge capacities of 1220.3 and 1112.4 mA h g^{-1}, and the results indicate the excellent rate capability of *hCuOx* and *sCuOx*.

To further evaluate the electrochemical properties of the $CuC_2O_4{\cdot}xH_2O$, the Nyquist plot and corresponding equivalent circuit were studied [15, 36]. Figure 7c, d shows the electrochemical impedance spectra (EIS) of *hCuOx* and *sCuOx* electrode of fresh cells. A slope line at lower frequency is related to the Warburg resistance of ion diffusion [41] at the medium frequency, which can be ascribed to the charge-transfer resistance (R_{ct}) and the constant phase element (CPE) of the interface of electrode and electrolyte. The lower slope line of frequency is related to the Warburg resistance of ion diffusion at intermediate frequency, which can be attributed to the R_{ct} and the CPE of the electrode and electrolyte interface [35]. For the fresh cell, R_{ct} values of *hCuOx* and *sCuOx* are 433.5 and 308.1 Ω, respectively. This is why the initial discharge capacity of *sCuOx* is greater than *hCuOx*. After three cycles in the CV measurement, R_{ct} values of *hCuOx*

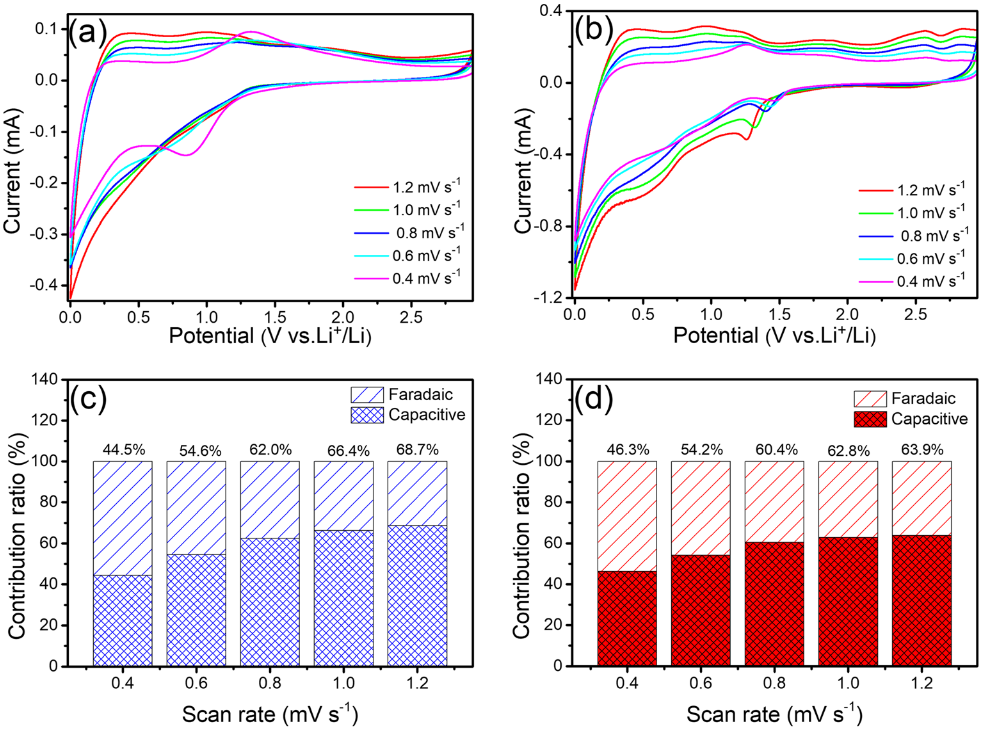

Fig. 8 CV curves of **a** *hCuOx* and **b** *sCuOx* at various scan rates, from 0.4 to 1.2 mV s^{-1}. **c** *hCuOx* and **d** *sCuOx* images express contribution ratio of the capacitive and faradaic at various scan rates

and *sCuOx* are 58.9 and 202.1 Ω, respectively. Thus, *hCuOx* is far better than *sCuOx* in R_{ct}.

The charge stored in a battery has two components: faradaic and capacitive. To confirm the quantitative relationship between faradaic and capacitive, CV analyses of *hCuOx* and *sCuOx* at various scan rates (0.4–1.2 mV s^{-1}) were carried out at 0.01–3.0 V (Fig. 8a, b). The faradaic current is proportional to the square root of voltage sweep rate, while the capacitive current is proportional to the voltage sweep rate [17]. Hence, faradaic contribution and capacitive can be expressed by the following equation [42]:

$$i(V) = k_1 v + k_2 v^{0.5} \tag{5}$$

or

$$i(V)/v^{0.5} = k_1 v^{0.5} + k_2 \tag{6}$$

where $i(V)$ is the current as a function of voltage, and $k_1 v$ and $k_2 v^{0.5}$ are amount to capacitive effects and diffusion-controlled reaction, respectively. According to Eq. (6), we can calculate the values of k_1 and k_2; consequently, the capacitive and faradaic current intensities separately. The contributions of faradaic and capacitive at different sweep rates are shown in Fig. 8c, d for 5 cycles. The general trend is that the higher the voltage scan rate, the higher the capacitive current. For *hCuOx* and *sCuOx*, the capacitance contribution rate can reach 68.7% and 63.9% at 1.2 mV s^{-1}, which indicates the irreplaceable role of the capacitive contribution in the total capacity. Therefore, the *hCuOx* and *sCuOx* have excellent lithium storage capacity as anode materials for lithium ion batteries.

Conclusions

In this work, we used a microwave-assisted hydrothermal and solvothermal method to fabricate the *hCuOx* and *sCuOx* anode materials' facile operation and rapid reaction. They have given distinct different morphologies (quasi-spherical and cotton shapes) explaining this surfactant-free method could be applied in green industrial process. SEM/TEM/BET characterizations revealed that *hCuOx* and *sCuOx* are nanoscale and mesoporous. The *hCuOx* and *sCuOx* manifest maximum discharge capacity of 1436.2 and 1688.1 mAh g^{-1}, respectively. The presence of crystallized water results in a rapid decrease in discharge capacity during the first four discharge cycles, but the remarkable lithium storage capacity of hydrated oxalates makes it impossible to ignore.

Funding information This research is supported by the National Natural Science Foundation of China (nos. 21404068 and 51502169).

References

1. Tarascon J-M, Armand M (2001) Issues and challenges facing rechargeable lithium batteries. Nature 414:359–367
2. Tarascon J-M (2010) Is lithium the new gold? Nat Chem 2:510
3. Wang B, Chen JS, Wu HB, Wang ZY, Lou XW (2011) Quasiemulsion-templated formation of alpha-Fe_2O_3 hollow spheres with enhanced lithium storage properties. J Am Chem Soc 133:17146–17148
4. Goodenough JB, Kim Y (2010) Challenges for rechargeable Li batteries. Chem Mater 22:587–603
5. Li H, Wang ZX, Chen LQ, Huang XJ (2009) Research on advanced materials for Li-ion batteries. Adv Mater 21:4593–4607
6. Wagemaker M, Mulder FM (2011) Properties and promises of nanosized insertion materials for Li-ion batteries. Acc Chem Res 46:1206–1215
7. Zhou ZR, Dong P, Wang DY, Liu M, Duan JG, Nayaka GP, Wang D, Xu CY, Hua YX, Zhang YJ (2019) Silicon-titanium nanocomposite synthesized via the direct electrolysis of SiO_2/TiO_2 precursor in molten salt and their performance as the anode material for lithium ion batteries. J Alloys Compd 781:362–370
8. Zhang XS, Zhou L, Huang MY, Yang CF, Xu YF, Huang JJ (2018) Synthesis of porous Si/C by pyrolyzing toluene as anode in lithium-ion batteries with excellent lithium storage performance. Ionics 1: 1–10
9. Chan CK, Zhang XF, Cui Y (2008) High capacity Li ion battery anodes using Ge nanowires. Nano Lett 8:307–309
10. Zaghib K, Simoneau M, Armand M, Gauthier M (1999) Electrochemical study of $Li_4Ti_5O_{12}$ as negative electrode for Li-ion polymer rechargeable batteries. J Power Sources 81:300–305
11. Park MS, Wang G, Kang Y, Wexler D, Dou S, Liu H (2007) Preparation and electrochemical properties of SnO_2 nanowires for application in lithium-ion batteries. Angew Chem Int Ed 46:750–753
12. Hu CY, Guo J, Wen J (2012) Hierarchical nanostructure CuO with peach kernel-like morphology as anode material for lithium-ion batteries. Ionics 19:253–258
13. Reddy MV, Subba GV, Chowdari BV (2013) Metal oxides and oxysalts as anode materials for Li ion batteries. Chem Rev 113: 5364–5457
14. Sun HY, Ahmad M, Zhu J (2013) Morphology-controlled synthesis of Co_3O_4 porous nanostructures for the application as lithium-ion battery electrode. Electrochim Acta 89:199–205
15. Ang WA, Cheah YL, Wong CL, Hng HH, Madhavi S (2015) One-pot solvothermal synthesis of $Co_{1-x}Mn_xC_2O_4$ and their application as anode materials for lithium-ion batteries. J Alloys Compd 638: 324–333
16. León B, Pérez CV, Tirado JL (2012) New mixed transition metal oxysalts as negative electrode materials for lithium-ion batteries. Solid State Ionics 225:518–521
17. López MC, Tirado JL, Pérez VC (2013) Structural and comparative electrochemical study of M(II) oxalates, M = Mn, Fe, Co, Ni, Cu, Zn. J Power Sources 227:65–71
18. Ang WA, Gupta N, Prasanth R, Madhavi S (2012) High-performing mesoporous iron oxalate anodes for lithium-ion batteries. ACS Appl Mater Interfaces 4:7011–7019
19. Wu XH, Guo JH, McDonald MJ, Li SG, Xu BB, Yang Y (2015) Synthesis and characterization of urchin-like $Mn_{0.33}$ $Co_{0.67}$ C_2O_4 for Li-ion batteries: role of SEI layers for enhanced electrochemical properties. Electrochim Acta 163:93–101
20. Xu JM, He L, Liu H, Han T, Wang YJ, Zhang CJ (2015) Controlled synthesis of porous anhydrous cobalt oxalate nanorods with high reversible capacity and excellent cycling stability. Electrochim Acta 170:85–91

21. Nacimiento F, Alcántara R, Tirado JL (2010) Cobalt and tin oxalates and PAN mixture as a new electrode material for lithium ion batteries. J Electroanal Chem 642:143–149
22. Zhang Y, Lu Z, Guo M, Bai Z, Tang B (2016) Porous CoC_2O_4 nanorods as high performance anode material for lithium ion batteries. Nano Lett 68:2952–2957
23. Oh HJ, Jo CH, Yoon CS, Yashiro H, Kim SJ, Passerini S, Sun Y, Myung ST (2016) Nickel oxalate dihydrate nanorods attached to reduced graphene oxide sheets as a high-capacity anode for rechargeable lithium batteries. NPG Asia Mater 8:270–278
24. Yeoh JS, Armer CF, Lowe A (2018) Transition metal oxalates as energy storage materials. A review. Mater Today Energy 9:198–222
25. Aragón MJ, León B, Serrano T, Vicente CP, Tirado JL (2011) Synergistic effects of transition metal substitution in conversion electrodes for lithium-ion batteries. J Mater Chem 21:10102–10107
26. Aragón MJ, León B, Pérez VC, Tirado JL (2008) Synthesis and electrochemical reaction with lithium of mesoporous iron oxalate nanoribbons. Inorg Chem 47:10366–10371
27. Aragón MJ, León B, Pérez B, Vicente CP, Tirado JL, Chadwick AV, Berko A (2009) Cobalt oxalate nanoribbons as negative-electrode material for lithium-ion batteries. Chem Mater 21:1834–1840
28. Ma J, Zhang XD, Chen KZ, Li GC, Han XD (2013) Morphology-controlled synthesis of hematite hierarchical structures and their lithium storage performances. J Mater Chem A 1:5545–5553
29. Shi SJ, Hua XY, Guo HT (2018) Microwave-assisted one-pot synthesis of SnC_2O_4/graphene composite anode material for lithium-ion batteries. Ceram Int 44:13495–13501
30. Holzwarth U, Gibson N (2011) The Scherrer equation versus the "Debye-Scherrer equation.". Nat Nanotechnol 6:534–534
31. Behnoudnia F, Dehghani H (2013) Copper(II) oxalate nanospheres and its usage in preparation of $Cu(OH)_2$, Cu_2O and CuO nanostructures: synthesis and growth mechanism. Polyhedron 56:102–108
32. Sun CL, Wu YD, Mei DJ, Doert T (2018) $Bi_2(IO_3)(IO_6)$: first combination of $[IO_3]^-$ and $[IO_6]^{5-}$ anions in three-dimensional framework. Solid State Sci 77:37–43
33. Ang WA, Cheah YL, Wong CL, Prasanth R, Hng HH, Madhavi S (2013) Mesoporous cobalt oxalate nanostructures as high-performance anode materials for lithium-ion batteries: ex situ electrochemical mechanistic study. J Phys Chem C 117:16316–16325
34. Kang WP, Shen Q (2013) The shape-controlled synthesis and novel lithium storage mechanism of as-prepared $CuC_2O_4 \cdot xH_2O$ nanostructures. J Power Sources 238(2013):203–209
35. Huang XH, Wang CB, Zhang SY, Zhou F (2011) CuO/C microspheres as anode materials for lithium ion batteries. Electrochim Acta 56:6752–6756
36. Gong YM, Zhao JC, Wang H, Xu J (2018) $CuCo_2S_4$/reduced graphene oxide nanocomposites synthesized by one-step solvothermal method as anode materials for sodium ion batteries. Electrochim Acta 292:895–902
37. Yang F, Li WY, Tang B (2018) Two-step method to synthesize spinel Co_3O_4-$MnCo_2O_4$ with excellent performance for lithium ion batteries. Chem Eng J 334:2021–2029
38. Liu BG, Peng JH, Zhang LB, Srinivasakannan C, Huang M, Zhang ZB, Guo SH (2011) Coupling and absorbing behavior of microwave irradiation on the $Co(C_2O_4) \cdot 2H_2O$:Co_3O_4 system. J Taiwan Inst Chem Eng 42:92–96
39. Ding HH, Yang JX, Ma SY, Yigit N, Xu JL (2018) Large dimensional CeO_2 nanoflakes by microwave-assisting synthesis: lamellar nano-channel and surface oxygen vacancies promoted catalytic activity. ChemCatChem 10:4100–4108
40. She WC, Luo K, Zhang CY, Wang G, Geng YY, Li L, He B, Gu ZW (2013) The potential of self-assembled, pH-responsive nanoparticles of mPEGylated peptide dendron-doxorubicin conjugates for cancer therapy. Biomaterials 34:1613–1623
41. Xiang YY, Wang Z, Qiu WJ, Guo ZR, Liu D, Qu DY, Xie ZZ, Tang HL, Li JS (2018) Interfacing soluble polysulfides with a SnO_2 functionalized separator: an efficient approach for improving performance of Li-S battery. J Membr Sci 568:380–387
42. Liu TC, Pell WG, Conway BE, Roberson SL (1998) Behavior of molybdenum nitrides as materials for electrochemical capacitors comparison with ruthenium oxide. J Electrochem Soc 145:1882–1888